Correlative single-cell X-ray tomography and X-ray fluorescence imaging

Zihan Lin[1,6], Xiao Zhang[1,6], Purbasha Nandi[1], Yuewei Lin[2], Liguo Wang[3], Yong Chu[4], Timothy Paape[1,5], Yang Yang[4,*], Xianghui Xiao[4,*], Qun Liu[1,4,*]

[1]Biology Department, [2]Computational Science Initiative, [3]LBMS, [4]NSLS-II, Brookhaven National Laboratory, Upton, New York, USA. [5]U.S. Department of Agriculture's Agricultural Research Service at Children's Nutrition Research Center, Houston, Texas, USA.

[6]These authors contributed equally to the work: Z. L., X. Z.

*Correspondence to: Y.Y.: yyang@bnl.gov, X.X.: xiao@bnl.gov, or Q.L.: qunliu@bnl.gov

Abstract:

X-ray tomography and x-ray fluorescence imaging are two non-invasive imaging techniques to study cellular structures and chemical element distributions, respectively. However, correlative X-ray tomography and fluorescence imaging for the same cell has yet to be routinely realized due to challenges in sample preparation and X-ray radiation damage. Here we report an integrated experimental and computational workflow for achieving correlative multi-modality X-ray imaging of a single cell. The method consists of the preparation of radiation-resistant single-cell samples using live-cell imaging-assisted chemical fixation and freeze-drying procedures, targeting and labeling cells for correlative x-ray tomography and x-ray fluorescence measurement, and computational reconstruction of the correlative and multi-modality images. With X-ray tomography, cellular structures including the overall structure and intracellular organelles are visualized, while X-ray fluorescence imaging reveals the distribution of multiple chemical elements within the same cell. Our correlative method demonstrates the feasibility and broad applicability of using X-rays to understand cellular structures and the roles of multiple chemical elements and related proteins in signaling and other biological processes.

Main:

Cells are the building blocks of living organisms. X-ray has deep-penetration power and is ideal for non-invasive imaging of cells at nanometer resolutions [1,2]. Transmission X-ray microscopy (TXM) tomography and X-ray scanning fluorescence imaging (XSF) are two nanometer-resolution imaging techniques capable of studying cellular structure and function in high spatial resolution. TXM is analog in its configuration to optical bright-field microscopy, utilizing a condenser to focus X-rays onto the sample and employing a zone plate as an X-ray objective lens to magnify images for full-field tomographic imaging [3,4]. Meanwhile, XSF imaging operates as a spectroscopic technique based on scanning, utilizing element-specific X-ray fluorescence spectra to map multiple chemical elements [5-7]. The two methods complement each other, where TXM provides the overall cellular and subcellular structures while XSF imaging generates elemental maps crucial for understanding element-related uptake, metabolism, and cellular localization.

Both X-ray imaging modalities have found extensive applications in biological research [3,5,8]. TXM utilizes either absorption or phase contrast for imaging biological cells. Soft X-rays at energy within the water window (183-530 eV) exhibit a larger mass absorption cross-section difference for carbon and nitrogen relative to water, thus creating absorption contrast for tomographic imaging of hydrated cells [1,9]. However, these soft X-rays are also associated with high parasitic X-ray absorption and radiation damage, necessitating the use of cryofixation and data collection at cryogenic temperatures [9]. Soft X-rays are also limited to a short focal length and samples thinner than 20 μm and thus, large cells such as some plant and animal cells may be challenging for soft X-ray tomography. In comparison, hard X-rays with an energy of 5 keV or higher possess a smaller cross-section but generate much less radiation damage while penetrating to great deeper, e.g. 1 mm for 10 keV x-rays [10]. Hard X-rays have been utilized to study cellular structures of unstained MC3 preosteoblasts [11] and fission yeast cells [12]. Due to the small cross-section difference between carbon, nitrogen, and water, the absorption contrast is very low for imaging biological cells. Hence, previous researchers preferred to use phase contrast mechanisms by a Zernike phase plate to create a phase delay between absorbed and scattered X-rays [11,12]. To enhance the contrast for hard X-ray imaging, staining cells using

heavy metals such as osmium, lead, and uranyl is generally required, but such a method limited the resolution and caused stain-related artifacts [12].

XSF is highly sensitive and capable of detecting elemental distributions in a sample at sub-ppm levels. Unlike other methods, XSF does not require the use of external markers or tags, enabling simultaneous detection of multiple elements with exceptional resolution using a highly focused X-ray beam [5,6]. This characteristic makes XSF suitable to probe and differentiate compositions of both metal and non-metal elements inside cells, thereby aiding in the understanding of their roles in signaling, homeostasis, and other cellular functions. As hard X-rays can detect biological elements with an atomic number of 15 (phosphorus) or higher and are insensitive to water, both hydrated and dehydrated samples have been employed for XSF [13-15]. XSF has been utilized to study cellular functions of metals, for example, zinc in leaf cells [16], copper in neuronal cells [17], and calcium, phosphorus, and iron in algae [18].

Although it is attractive to image the same cells using multiple X-ray modalities [19,20], challenges exist in developing suitable sample preparation protocols to optimize contrast and mitigate the radiation damage associated with the measurement of the same cells, as well as data correlation between the two imaging modalities. Addressing these challenges is crucial to facilitate the routine application of these correlative techniques for precise imaging at cellular and subcellular levels. Here we developed a single-cell X-ray imaging workflow that encompasses sample preparation, targeting, multi-modality data acquisition, and computational alignments of multi-modality image data at nanometer resolutions. Our method offers a reliable and practical approach for obtaining the structure and chemical information of a single cell with nanometer-level resolution. The results of our research pave the way for the broad application of hard X-rays for correlative characterization of cell structure and function, opening up new possibilities for advanced biological investigations.

Results

A single-cell multi-modality X-ray imaging workflow

HEK293 cells were utilized in this study to demonstrate the workflow. Cells are fragile and their manipulation and targeting require the use of compatible sample holders and experimental setups across various imaging modalities. **Fig. 1** depicts the devised workflow for achieving single-cell-level correlative multi-modal imaging. To begin, an X-ray transparent Si_3N_4 membrane is used for growing cells (**Fig. 1a**). Subsequently, the grown cells are chemically fixed using paraformaldehyde (PFA) to preserve cellular structure and morphology (**Fig. 1b**). The cells are then dehydrated by freeze-drying [21] to retain cell structure while gradually depleting water through sublimation. Fixed cells are manually blotted using filter paper and rapidly plunge-freeze into liquid ethane using a Vitrobot (Thermo Fisher Scientific Inc.), and later are transferred into liquid nitrogen (**Fig. 1c**). The vitrified cells were then freeze-dried (**Fig. 1d**) and imaged using a confocal light microscope for targeting and labeling cells (**Fig. 1e**). The labeled cells are measured first with TXM then with XSF (**Fig. 1f**). TXM and XSF data were processed separately to obtain respective 3D tomograms and 2D chemical maps (**Fig. 1g**). Two sets of images are then computationally aligned to generate the final integrated images (**Fig. 1h**). This integrated workflow provides a comprehensive and detailed visualization of the cellular structure and the distribution of chemical elements within the same cell.

Single-cell sample preparation and labeling

Freeze drying plays a critical role in preparing cell samples for XSF experiments [22,23]. However, XSF imaging is limited to detecting fluorescence-emitting chemicals such as Zn and Ca while does not provide information about the carbon-, nitrogen, and oxygen-rich cellular structure. Consequently, fixation conditions optimized for XSF imaging may not be optimal for the correlated TXM, which aims to reveal the three-dimensional cellular structure. To address this issue, the fixation conditions were optimized using 4% paraformaldehyde (PFA), a routinely employed fixative for cell fixation before immunolabeling and x-ray fluorescence imaging [23,24]. The goal was to strike a balance between maintaining the integrity of the cellular structure for TXM and preserving chemical elements for subsequent XSF imaging. Upon the addition of 4% PFA to the cultured cells, the entire fixation process was continuously monitored using a Nanolive imaging system at 30-second intervals over two hours (**Supplementary movie 1**). The snapshots before and after fixation are shown in **Supplementary Fig. 2a**. No significant

changes were observed in the fixed cells compared to the initial time point (0 min). Furthermore, we didn't observe membrane blebbing or loss of cytoplasmic content during the entire two-hour fixation period [25].

Subsequently, PFA-fixed cells with fixation durations of 15 min, 60 min, and 120 min were subjected to vitrification and freeze-drying. To enable the performance of both TXM and XSF imaging on a single cell, the cell density on the Si3N4 membrane was optimized to ensure sufficient separation between cells. Additionally, a confocal microscope was used to capture both the overall view and zoomed-in images (**Supplementary Fig. 2b**). The cells were labeled in the optical images, and the labeled locations of the cells were utilized to target the same cells in TXM and XSF experiments. This multi-resolution imaging approach can be employed to label and target any cells on a Si3N4 membrane.

Hard X-ray tomography

TXM experiments were conducted at the Full-field X-ray Imaging (FXI) beamline of the National Synchrotron Light Source II (NSLS-II) at Brookhaven National Laboratory (BNL). The FXI beamline is equipped with a Transmission X-ray Microscopy (TXM) capable of rapid measurements at 30 nm spatial resolution in less than one minute [26]. To minimize X-ray radiation damage to the samples, an optical telescope, coaligned with the X-ray beam, was utilized for target cell identification and pre-alignment. This ensured that the samples were not exposed to the X-ray beam until the actual TXM data collection started. The TXM operates within an x-ray energy range from 5 to 11 keV. Taking into account the optimal imaging contrast and the flux, we conducted all the tomography experiments at 7 keV.

The tomograms of the target cells were reconstructed using TXM sandbox [27] and visualized with IMOD [28]. **Figs. 2a and 2b** display the volume rendering of a cell's tomogram, revealing a well-defined plasma membrane encompassing rich cellular structures. The shape of the cell matches the confocal microscope image depicted in **Supplementary Fig. 2b**. More structure details of this cell can be visualized in **Supplementary Movie 2**. Within the cell, two elongated organelles of about 500-800 nm in size are visible close to the plasma membrane (**Fig. 2c, d**). Based on their appearance,

these organelles are likely bilayer endosome/lysosome (**Fig. 2c**) or multilayer mitochondrion (**Fig. 2c**). In addition, we observed double membrane structures (**Fig. 2d**), i.e. plasma membrane and intracellular membrane. By considering their length and smooth curvature of the internal membrane, we assigned it as the nucleus membrane. Upon viewing the cell from the top on the Si_3N_4 membrane, a few small vesicles of 300 nm can be identified (**Fig. 2e**). Based on the size and high x-ray contrast, we assigned these vesicles as lipid droplets. These lipid droplets exhibit spherical shapes, contrasting with the surrounding air. Another compartment membrane structure is displayed between the plasma membrane and intracellular membrane (**Fig. 2e**). However, we were not able to rationally assign the membrane structure to any known organelle. Based o the features of the nucleus membrane and high contrast from chromatin, we were able to segment the nucleus manually inside the cell (**Fig. 2f, g**). The 2D views of the 3D volume along three orthogonal planes demonstrate the positioning of the segmented nucleus within the cell (**Fig. 2g**).

X-ray fluorescence imaging

TXM X-ray tomography is an effective method for visualizing cellular structures. Nonetheless, due to low abundance, it cannot reveal the chemical element of trace micronutrient metals such as Zn, Fe, Cu, and Ca, essential for proper cell function. To investigate the elemental distributions within the same cell, we performed XSF measurement at the Submicron Resolution X-ray Spectroscopy (SRX) beamline at NSLS-II. In order to precisely locate the same cell, we utilized the in-line optical microscope at SRX to identify and center the cell for the collection of raster scanning x-ray fluorescence data. To achieve high spatial resolution, we utilized a beam size of approximately 100 nm and a step size of 100 nm at an x-ray energy of 12 keV.

Figure 3 presents the chemical mapping of six common chemical elements: Ca, Cl, Cu, Fe, P, and Zn. Among these, zinc was predominantly localized in the center of the cell, i.e. nucleus, with its concentration gradually decreasing but remaining within the nucleus region. Phosphorus is mostly enriched in the chromatin/nucleus, consistent with its co-localization with zinc, which is known to bind to transcription factors to regulate gene

transcription in the nucleus [29]. Interestingly, calcium appears to be distributed in separate regions of various sizes of about 1 μm or smaller in diameter. Given calcium's cytotoxic nature, it is typically confined to calcium stores [30]. Therefore, it is likely that these calcium-rich regions correspond to calcium stores associated with ER or mitochondria. Copper seems to be attached to the outside of the phosphorus and zinc but extends beyond the zinc map (**Supplementary Fig. 4**). The chloride distribution appears to resemble that of zinc and phosphorus. Unlike other elements, which remain immobile during the fixation process, chloride is soluble within the cell. It remains unclear why it remained in the nucleus despite the PFA fixation.

Correlation of X-ray tomography and fluorescence data

We established a correlation between the 3D tomography image and the 2D fluorescence data obtained from the same cell, displaying chemical element localization within the cell. To achieve accurate alignment between both images, additional XSF data were acquired by performing rotations at -15°, 25°, and 55° along the z-axis, consistent with the rotation axis employed at the FXI. To generate correlation maps, the 3D tomogram was appropriately rotated to match the orientation of the 2D fluorescence maps. Subsequently, we performed the total projections of the segmented cell plasma membrane and nucleus onto their respective 2D fluorescence maps (**Fig. 4 and Supplementary Fig. 5)**. These multi-orientation XSF data facilitated the precise overlay of fluorescence signals onto the corresponding cellular structures, enabling the visualization and examination of chemical element distribution within the cell.

Collecting XSF data at multiple orientations has proven instrumental in accurately localizing chemical elements within the X-ray tomogram. For instance, the four orientations utilized for the calcium maps indicate that these calcium stores are situated close to, yet outside of the nucleus, suggesting their association with the rough ER or mitochondria. Interestingly, copper is accumulated at one side of the cell and is also close to, but outside of, the nucleus. The elongated shape of the Cu map along the nucleus membrane, suggests its localization to rough ER or Golgi apparatus. Copper and calcium have been reported to be involved in the function of both mitochondria and the ER, raising intriguing questions for future studies [31,32]. The correlative and non-invasive multi-

modality imaging of the same cell provides a tool to further characterize element distribution inside a cell which may not be possible using other imaging tools.

Radiation damage

To assess the X-ray-caused radiation damage, a series of six consecutive X-ray tomography scans were performed on the same cell, employing different experimental conditions such as exposure time, rotation speed, and X-ray energy. Subsequently, a 7th scan was conducted with the same parameters as the initial one. The resulting tomograms were reconstructed using TXM sandbox and IMOD, employing the same reconstruction parameters and post-processing filters. The first and the last tomograms were chosen for comparative analysis (**Fig. 5**). The results indicate that the repeated tomography data collection induced the cell-volume shrinkage by approximately 5% along each dimension (**Fig 5 and supplementary Fig. 6**). In addition, high-resolution features seen in the first scan were blurred or even disappeared in the 7th scan. The estimated X-ray dose for each scan was about 5 MGy determined by using the program RADDOSE3D [33]. To quantify the progressive change in cell volume with respect to repeated X-ray scans and radiation damage, we measured the alternation in cell dimension as shown in **Supplementary Fig. 6**. Notably, significant changes in cell volume were observed after the first three scans, equivalent to an X-ray dose of **15** MGy. We suggest that for single-cell X-ray tomography, the total dose should be limited to **15** MGy or lower.

Discussion

In this work, we developed an experimental and computational workflow that allows for the correlation of two distinct bioimaging modalities: nano-TXM and nano-XSF imaging. This approach enables the investigation of intracellular structures and chemical-element distributions within the same cells. The fast TXM serves as an effective screening tool to identify cells with interesting structural features. The selected cells are then scanned with XSF to obtain elemental maps, providing complementary information about the distribution of specific elements within the cell. In addition, the tomogram of a cell serves as a spatial framework, allowing for the precise localization of elemental maps within the context of cellular structure. The correlation between X-ray tomography and fluorescence

provides valuable insights into cellular compositions (**Fig. 4**). For instance, phosphorus, a key component of DNA and chromatin, enriches the central region of the cell, corresponding to the segmented nucleus. Interestingly, zinc, which exhibits stronger fluorescence signals compared to phosphorus, co-localized with phosphorus in the same cellular region. This suggests a potential involvement of zinc in DNA-related biological activities, supported by previous research [34].

The abundance of each chemical element within a cell has a wide range of distributions, resulting in XSF signals with varying intensities. Further optimization of detector sensitivity and data collection conditions may increase the signal-to-noise ratios for better-detecting low-concentration trace elements such as Fe, Mn, Co, and Ni, which are essential to support proper cell function [35]. During our cell culture and sample preparation, no additional chemical elements were introduced. The observed distribution and localization of chemical elements within the HEK293 cell likely reflect their physiological concentrations and localization. In addition to correlating two X-ray imaging modalities, further correlation with fluorescence optical microscopy will provide additional insights into the function of transporter proteins associated with these elements. For instance, overexpression or knockdown of zinc transporters [36,37] in the plasma membrane and intracellular membranes of a cell mode can shed light on their role in regulating zinc homeostasis and its physiological and pathological implications.

Radiation damage presents a significant challenge in achieving high-resolution imaging of biological samples [38,39]. Chemical fixation has proven to be an effective method for preserving biological samples and mitigating radiation damage [23,40]. By employing chemical fixation, hard X-rays were able to be performed on room-temperature cells while preserving intracellular features [13,25,41,42]. To prepare radiation-resistant cell samples, we employed an extended fixation time of 2 hours using paraformaldehyde (PFA) followed by freeze-drying to remove water. In our initial tests, insufficient PFA fixation (15 minutes) resulted in bubbles or the loss of internal features during TXM analysis. Live-cell imaging provides an ideal approach to monitor the fixation process and identify optimal conditions suitable for multi-modality X-ray experiments. We hypothesize that the longer fixation

duration allowed for better penetration of PFA into intracellular organelles including the nucleus for complete fixation of cellular contents.

In other techniques such as X-ray crystallography and cryo-electron microscopy (cryo-EM), the recommended radiation doses for biological samples are 20 MGy for frozen-hydrated samples and 0.38 MGy for room-temperature hydrated samples [41,43]. In our room temperature TXM experiments, we conducted radiation damage tests using repeated scans, with each scan delivering a dose of approximately 5 MGy. Remarkably, we observed no significant overall cell volume shrinkage even after three scans, resulting in an accumulated dose of 15 MGy, which is significantly higher than that used for hydrated cells. Since the spatial resolution in TXM is about two orders of magnitude lower than in X-ray crystallography and cryo-EM, it is reasonable to assume the tolerance to X-ray dose in TXM is higher than the thresholds used in X-ray crystallography and cryo-EM. Nonetheless, a long fixation time in the sample preparation is recommended for TXM measurements to alleviate the radiation damage challenge. Exploring the precise relationship between fixation time and X-ray damage could be an intriguing avenue for future studies.

In our multimodal experiments, we conducted XSF measurements after performing seven scans for TXM data collection. However, we didn't consider the cumulative dose prior to the XRF experiments. Consequently, we observed a slight discrepancy between the XRF maps obtained after the seventh scan and the X-ray tomography data from the initial scan, attributed to cell shrinkage and radiation damage (**Fig. 5 and supplementary Fig. 6**). XRF imaging primarily detects chemical elements bound to proteins and nucleic acids, making it less sensitive to radiation damage compared to fine cellular structures. Retrospectively, a more rational experimental strategy would have been to allocate the total dose of 15 MGy between TXM and XSF data acquisition for better results. Nevertheless, our analysis of radiation damage underscores the significance of careful

planning and the selection of appropriate experimental conditions for successful correlative multimodal X-ray experiments.

Our method and workflow were developed specifically for HEK293 cells, our approach is generalizable and can be applied to identify optimal sample preparation conditions for other cell types. In our sample preparation, we deliberately avoided the use of contrast-enhancing metals, such as osmium, lead, and uranyl, as they have the potential to introduce additional artifacts to the cellular structure and interfere with the XSF analysis. The current TXM results obtained in our study primarily relied on absorption contrast, which provides limited differentiation between different organelles. To enhance contrast in future experiments, we propose the implementation of techniques such as Zernike-like phase plate phase contrast [12]. This method can potentially improve the visibility and distinction of cellular structures by introducing phase shifts in the X-ray beam, leading to enhanced contrast and improved resolution in TXM imaging.

Methods

Visualization of the chemically fixed cell using live-cell imaging

Adherent HEK293 cell (ATCC Cat# CRL-1573) was cultured in Dulbecco's Modified Eagle's Medium (DMEM) supplemented by 10% (v/v) fetal bovine serum and 100 units/ml of penicillin-streptomycin (Cat# 15140122, Thermo Fisher). Cell sub-culturing was performed twice a week to maintain cell viability and proliferation. To visualize cell growth, a 1 ml suspension of cells at a concentration of $1x10^5$ cells/ml was seeded onto an Ibidi µ-Dish 35 mm, low (Cat#80136, Ibidi) and allowed to grow overnight. Cell growth was visually inspected by a light microscope before chemical fixation.

To visualize the chemical fixation process, a 4% (v/v) paraformaldehyde (PFA) solution was diluted from 16% stock (Cat# 50-980-487, Electron Microscopy Sciences) by 1X Gibco™ DPBS (Cat# 14190-136, Thermo Fisher). Culture media was discarded carefully followed by two washes, each with 1 ml of 1X Gibco™ DPBS. Subsequently, the fixation solution was gently added from the side of the well to cover the middle area of the dish. A transparent lid was placed on the dish, and the dish was then placed in a stage-CO_2

incubator on a 3D Cell Explorer-fluo light microscope (Nanolive). The incubator was operated at 37°C, 5% CO_2, and 100% humidity. The Nanolive microscope was operated to perform real-time imaging for 2 hours, with images captured at 30-second intervals.

Cell culture on Si_3N_4 membrane substrate

The procedure for cell seeding on Si_3N_4 membranes was adapted from [21] with the following modifications. Si_3N_4 membranes (Cat# NX5200E, Norcada) were glow-discharged using a PELCO easiGlow Glow Discharge Cleaning System (Tedpella) under conditions at 30 mA for 30 seconds. Subsequently, they were treated with 10 µl of poly-L-lysine (Cat# 25988-63-0, Sigma) and incubated in a cell-culture incubator (37 °C and 8% CO_2) for 25 min. Afterward, the membranes were washed 3 times for 10 seconds each with sterile MilliQ water and vacuum-dried overnight. Then, the membranes were seeded with 10 µl of $1x10^6$ cells/ml in a Falcon 24-well cell culture plate (Cat# 353047, Fisher Scientific) and the plate was incubated in the cell-culture incubator (37 °C and 8% CO2) for 25 minutes. Furthermore, 500 µl of cell culture media was gently added from the side of the well to ensure coverage of the membranes. The plate was then stored in the incubator for overnight cell culture.

Chemical fixation

The chemical fixation procedure was modified from [21,25]. Cell culture media was removed from the well containing the Si_3N_4 membrane with attached cells. Subsequently, the Si_3N_4 membrane was washed with 1 ml DPBS twice and fixed for 2 hours with 1 ml of 4% PFA as previously described. After fixation, membranes were washed twice with 1 ml of ammonium acetate (150 mM, pH 7.4) to remove residual fixatives.

Plunge-freezing and freeze-drying

To prepare the samples for freeze-drying, samples were blotted manually by using filter paper to remove liquid on the frame and on the back of the Si_3N_4 window. The plunge-freezing was performed using a Mark IV Vitrobot (Thermo Fisher). Frozen samples were then transferred into a pre-cooled 2-ml screw cap tube (Cat# HS10060, Millipore Sigma) for freeze-drying. After the FreeZone 12 Liter -84C Console Freeze Dryer (Cat#

711211110, Labconco) was set to –80°C with a vacuum level of 0.05 mbar, the sample tubes were quickly transferred into a freeze-drying container preloaded with liquid nitrogen. The container was swiftly connected to the freeze-drying machine while the vacuum valve was turned from off to on. The samples were subjected to freeze-drying for 2 days to ensure complete removal of water.

Cell labeling for correlated multimodality data acquisition

To obtain multi-modality data at multiple X-ray beamlines, it is necessary to perform cell imaging and labeling. We used a Leica TCS SP5 (Leica Microsystems Inc., Deerfield, IL, USA) to provide an overall view of cells on the Si_3N_4 membranes as well as to label cells for correlated X-ray imaging data acquisition. The freeze-dried sample was gently put upside down on the center of a µ-Dish before imaging. A 10x objective lens was employed to survey the cells present on the membranes. Once a specific cell of interest was identified and labeled, the objective lens was switched to 50x magnification to capture high-resolution images of the labeled cells, serving as a reference for subsequent X-ray data collection.

X-ray tomography data collection

The samples were manually mounted onto the FXI beamline data collection stage, and the target cell was identified using a telescope that precisely aligned with the X-ray beam. The TXM tomography data were acquired using X-rays at 7 KeV. Two different exposure schemes were employed: 0.1 sec exposure at a speed of 3°/ sec and 0.2 sec exposure at a speed of 1.5°/sec. For each scheme, three data sets were collected with a defocus of 0, 50, and 100 µm. To assess the extent of radiation damage, an additional data set was collected with the same condition as used for the first data set.

Correlated XSF data collection

The freeze-dried samples were transferred and positioned at the SRX beamline [44] for room temperature XSF measurements following the FXI TXM experiments. At SRX, a pair of rhodium-coated KB (Kirkpatrick–Baez) mirrors is used to focus the X-ray beam down to 190 nm (H) x 230 nm (V) nm. By employing an in-line optical light microscope

(VLM), we were able to locate the same cell for correlative composition mapping. The focused beam was used to raster scan the samples, allowing for the measurement of elements of biological significance. Cells were fly scanned with 0.1 μm step size with 0.1 s dwell time, with the photon energy at 12 keV and flux of about 4.5 x 10^{11} ph/s. A Vortex 7-element silicon drift detector (Hitachi, Ltd.) was located at an angle of 75° with respect to the incident beam to capture the fluorescence emission. The obtained spectra were subsequently analyzed using the open software PyXRF [45] to generate elemental distribution maps for each element.

X-ray imaging data analysis

X-ray tomograms were reconstructed using TXM-Sandbox [27] and IMOD [28]. As described in TXM-sandbox, the rotation center position was first identified in TXM-sandbox's "Trial Center" mode in the raw images. Various filter parameters, reconstruction algorithms and parameters were tested under this mode to find the optimal reconstruction condition. Then a full image reconstruction was performed under "Volume Reconstruction" mode. After the reconstruction, phase retrieval, stripe removal, and median filters were used to reduce the artifacts caused by imperfect image collection.

The cell membrane was segmented semiautomatically using FIJI [46] (https://imagej.net/software/fiji/) and IMOD. First, a Canny edge detector was employed to enhance the boundaries within a predefined region of interest in the image, followed by the application of thresholding to convert these enhanced boundaries into binary masks. The threshold value was chosen to retain only the cell membrane boundaries while eliminating the nucleus membrane boundaries. Afterward, image binary opening and closing operations were conducted to eliminate smaller noise objects. First, a Canny edge detector was used to enhance the cell membrane region and then thresholding was used to convert the enhanced membrane region to binary masks. The resultant membrane masks were converted to 3D IMOD model using "imodmop" and "imodauto"

commands. The cell nucleus was segmented manually using IMOD. The resultant 3D model was visualized with IMOD and Napari [47] (http://narpari.org).

Correlation of X-ray tomography and fluorescence images

The reconstructed 3D X-ray tomograms were first projected into 2D projection maps along the 4 different angles (-15°, 0°, 25°, 55°). Then 2D rigid image registration (translation + rotation) was performed with FIJI [46] (https://imagej.net/software/fiji/) on 2D X-ray projection image and 2D fluorescent image separately for four different angles. The registered images from two imaging modalities were overlaid and visualized with Napari.

References

1 Le Gros, M. A., McDermott, G. & Larabell, C. A. X-ray tomography of whole cells. ***Curr Opin Struct Biol*** 15, 593-600, (2005).

2 Ou, X., Chen, X., Xu, X., Xie, L., Chen, X., Hong, Z., Bai, H., Liu, X., Chen, Q., Li, L. & Yang, H. Recent Development in X-Ray Imaging Technology: Future and Challenges. ***Research (Wash D C)*** 2021, 9892152, (2021).

3 Andrews, J. C., Meirer, F., Liu, Y. J., Mester, Z. & Pianetta, P. Transmission X-Ray Microscopy for Full-Field Nano Imaging of Biomaterials. ***Microsc Res Techniq*** 74, 671-681, (2011).

4 Spence, S., Lee, W. K., Lin, F. & Xiao, X. H. Transmission x-ray microscopy and its applications in battery material research-a short review. ***Nanotechnology*** 32, (2021).

5 Pushie, M. J., Sylvain, N. J., Hou, H., Hackett, M. J., Kelly, M. E. & Webb, S. M. X-ray fluorescence microscopy methods for biological tissues. ***Metallomics*** 14, (2022).

6 Paunesku, T., Vogt, S., Maser, J., Lai, B. & Woloschak, G. X-ray fluorescence microprobe imaging in biology and medicine. ***J Cell Biochem*** 99, 1489-1502, (2006).

7 Decelle, J., Veronesi, G., Gallet, B., Stryhanyuk, H., Benettoni, P., Schmidt, M., Tucoulou, R., Passarelli, M., Bohic, S., Clode, P. & Musat, N. Subcellular Chemical Imaging: New Avenues in Cell Biology. ***Trends in Cell Biology*** 30, 173-188, (2020).

8 Chen, J. H., Vanslembrouck, B., Loconte, V., Ekman, A., Cortese, M., Bartenschlager, R., McDermott, G., Larabell, C. A., Le Gros, M. A. & Weinhardt, V. A protocol for full-rotation soft X-ray tomography of single cells. ***STAR Protoc*** 3, 101176, (2022).

9 Larabell, C. A. & Nugent, K. A. Imaging cellular architecture with X-rays. ***Curr. Opin. Struc. Biol.*** 20, 623-631, (2010).

10 Hémonnot, C. Y. & Köster, S. Imaging of biological materials and cells by X-ray scattering and diffraction. ***ACS nano*** 11, 8542-8559, (2017).

11 Stampanoni, M., Mokso, R., Marone, F., Vila-Comamala, J., Gorelick, S., Trtik, P., Jefimovs, K. & David, C. Phase-contrast tomography at the nanoscale using hard x rays. ***Physical Review B*** 81, 140105, (2010).

12 Yang, Y., Li, W., Liu, G., Zhang, X., Chen, J., Wu, W., Guan, Y., Xiong, Y., Tian, Y. & Wu, Z. 3D visualization of subcellular structures of Schizosaccharomyces pombe by hard X-ray tomography. ***J Microsc*** 240, 14-20, (2010).

13 Jin, Q., Paunesku, T., Lai, B., Gleber, S. C., Chen, S. I., Finney, L., Vine, D., Vogt, S., Woloschak, G. & Jacobsen, C. Preserving elemental content in adherent mammalian cells for analysis by synchrotron-based x-ray fluorescence microscopy. ***J Microsc*** 265, 81-93, (2017).

14 Matsuyama, S., Shimura, M., Fujii, M., Maeshima, K., Yumoto, H., Mimura, H., Sano, Y., Yabashi, M., Nishino, Y., Tamasaku, K., Ishizaka, Y., Ishikawa, T. & Yamauchi, K. Elemental mapping of frozen-hydrated cells with cryo-scanning X-ray fluorescence microscopy. ***X-Ray Spectrom*** 39, 260-266, (2010).

15 Gramaccioni, C., Yang, Y., Pacureanu, A., Vigano, N., Procopio, A., Valenti, P., Rosa, L., Berlutti, F., Bohic, S. & Cloetens, P. Cryo-nanoimaging of Single Human Macrophage Cells: 3D Structural and Chemical Quantification. ***Analytical Chemistry*** 92, 4814-4819, (2020).

16 Vigani, G., Bohic, S., Faoro, F., Vekemans, B., Vincze, L. & Terzano, R. Cellular Fractionation and Nanoscopic X-Ray Fluorescence Imaging Analyses Reveal Changes of Zinc Distribution in Leaf Cells of Iron-Deficient Plants. ***Front Plant Sci*** 9, (2018).

17 Dodani, S. C., Domaille, D. W., Nam, C. I., Miller, E. W., Finney, L. A., Vogt, S. & Chang, C. J. Calcium-dependent copper redistributions in neuronal cells revealed by a fluorescent copper sensor and X-ray fluorescence microscopy. ***Proc. Natl. Acad. Sci. USA*** 108, 5980-5985, (2011).

18 Diaz, J., Ingall, E., Vogt, S., de Jonge, M. D., Paterson, D., Rau, C. & Brandes, J. A. Characterization of phosphorus, calcium, iron, and other elements in organisms at sub-micron resolution using X-ray fluorescence spectromicroscopy. ***Limnol Oceanogr-Meth*** 7, 42-51, (2009).

19 Yang, Y., Fus, F., Pacureanu, A., da Silva, J. C., De Nolf, W., Biot, C., Bohic, S. & Cloetens, P. Three-Dimensional Correlative Imaging of a Malaria-Infected Cell with a Hard X-ray Nanoprobe. ***Analytical Chemistry*** 91, 6549-6554, (2019).

20 Deng, J. J., Vine, D. J., Chen, S., Nashed, Y. S. G., Jin, Q. L., Phillips, N. W., Peterka, T., Rossc, R., Vogt, S. & Jacobsen, C. J. Simultaneous cryo X-ray ptychographic and fluorescence microscopy of green algae. ***Proc. Natl. Acad. Sci. USA*** 112, 2314-2319, (2015).

21 Bissardon, C., Reymond, S., Salome, M., Andre, L., Bayat, S., Cloetens, P. & Bohic, S. Cell Culture on Silicon Nitride Membranes and Cryopreparation for Synchrotron X-ray Fluorescence Nano-analysis. ***J Vis Exp***, (2019).

22 Finney, L. A. & Jin, Q. Preparing adherent cells for X-ray fluorescence imaging by chemical fixation. ***J Vis Exp***, (2015).

23 Li, Y., Almassalha, L. M., Chandler, J. E., Zhou, X., Stypula-Cyrus, Y. E., Hujsak, K. A., Roth, E. W., Bleher, R., Subramanian, H., Szleifer, I., Dravid, V. P. & Backman, V. The effects of chemical fixation on the cellular nanostructure. ***Exp Cell Res*** 358, 253-259, (2017).

24 Zu, Y., Tong, X. J., Wang, Z. X., Liu, D., Pan, R. C., Li, Z., Hu, Y. Y., Luo, Z., Huang, P., Wu, Q., Zhu, Z. Y., Zhang, B. & Lin, S. TALEN-mediated precise genome modification by homologous recombination in zebrafish. ***Nat. Methods*** 10, 329-+, (2013).

25 Huebinger, J., Spindler, J., Holl, K. J. & Koos, B. Quantification of protein mobility and associated reshuffling of cytoplasm during chemical fixation. ***Sci Rep*** 8, 17756, (2018).

26 Lee, W. K., Reininger, R., Loo, W., Gambella, R., O'Hara, S., Chu, Y. S., Zhong, Z. & Wang, J. FXI: a full-field imaging beamline at NSLS-II. ***Proc Spie*** 9592, (2015).

27 Xiao, X., Xu, Z., Lin, F. & Lee, W. K. TXM-Sandbox: an open-source software for transmission X-ray microscopy data analysis. ***J Synchrotron Radiat*** 29, 266-275, (2022).

28 Mastronarde, D. N. & Held, S. R. Automated tilt series alignment and tomographic reconstruction in IMOD. ***J. Struct. Biol.*** 197, 102-113, (2017).

29 Eide, D. J. Transcription factors and transporters in zinc homeostasis: lessons learned from fungi. ***Crit. Rev. Biochem. Mol. Biol.*** 55, 88-110, (2020).

30 Sammels, E., Parys, J. B., Missiaen, L., De Smedt, H. & Bultynck, G. Intracellular Ca2+ storage in health and disease: a dynamic equilibrium. ***Cell Calcium*** 47, 297-314, (2010).

31 Ruiz, L. M., Libedinsky, A. & Elorza, A. A. Role of Copper on Mitochondrial Function and Metabolism. ***Front Mol Biosci*** 8, 711227, (2021).

32 Ashby, M. C. & Tepikin, A. V. ER calcium and the functions of intracellular organelles. ***Semin Cell Dev Biol*** 12, 11-17, (2001).

33 Zeldin, O. B., Gerstel, M. & Garman, E. F. RADDOSE-3D: time- and space-resolved modelling of dose in macromolecular crystallography. ***J Appl Crystallogr*** 46, 1225-1230, (2013).

34 Beyersmann, D. & Haase, H. Functions of zinc in signaling, proliferation and differentiation of mammalian cells. ***Biometals*** 14, 331-341, (2001).

35 Zoroddu, M. A., Aaseth, J., Crisponi, G., Medici, S., Peana, M. & Nurchi, V. M. The essential metals for humans: a brief overview. ***J. Inorg. Biochem.*** 195, 120-129, (2019).

36 Pratt, E. P. S., Damon, L. J., Anson, K. J. & Palmer, A. E. Tools and techniques for illuminating the cell biology of zinc. ***Bba-Mol Cell Res*** 1868, (2021).

37 Kambe, T., Taylor, K. M. & Fu, D. Zinc transporters and their functional integration in mammalian cells. ***J. Biol. Chem.*** 296, 100320, (2021).

38 Baksh, P., Odstrcil, M., Parsons, A., Bailey, J., Deinhardt, K., Chad, J. E., Brocklesby, W. S. & Frey, J. G. in *Journal of Physics: Conference Series.* 012034 (IOP Publishing).

39 Howells, M. R., Beetz, T., Chapman, H. N., Cui, C., Holton, J., Jacobsen, C., Kirz, J., Lima, E., Marchesini, S. & Miao, H. An assessment of the resolution limitation due to radiation-damage in x-ray diffraction microscopy. ***Journal of electron spectroscopy and related phenomena*** 170, 4-12, (2009).

40 Hopwood, D. Fixatives and fixation: a review. ***Histochem J*** 1, 323-360, (1969).

41 de la Mora, E., Coquelle, N., Bury, C. S., Rosenthal, M., Holton, J. M., Carmichael, I., Garman, E. F., Burghammer, M., Colletier, J. P. & Weik, M. Radiation damage

and dose limits in serial synchrotron crystallography at cryo- and room temperatures. ***Proc. Natl. Acad. Sci. USA*** 117, 4142-4151, (2020).

42 Murk, J. L., Posthuma, G., Koster, A. J., Geuze, H. J., Verkleij, A. J., Kleijmeer, M. J. & Humbel, B. M. Influence of aldehyde fixation on the morphology of endosomes and lysosomes: quantitative analysis and electron tomography. ***J Microsc*** 212, 81-90, (2003).

43 Henderson, R. Cryoprotection of Protein Crystals against Radiation-Damage in Electron and X-Ray-Diffraction. ***P Roy Soc Lond B Bio*** 241, 6-8, (1990).

44 Nazaretski, E., Coburn, D. S., Xu, W., Ma, J., Xu, H., Smith, R., Huang, X., Yang, Y., Huang, L., Idir, M., Kiss, A. & Chu, Y. S. A new Kirkpatrick-Baez-based scanning microscope for the Submicron Resolution X-ray Spectroscopy (SRX) beamline at NSLS-II. ***J Synchrotron Radiat*** 29, 1284-1291, (2022).

45 Li, L., Yan, H., Xu, W., Yu, D. T., Heroux, A., Lee, W. K., Campbell, S. I. & Chu, Y. S. PyXRF: Python-Based X-ray Fluorescence Analysis Package. ***X-Ray Nanoimaging: Instruments and Methods Iii*** 10389, (2017).

46 Schindelin, J., Arganda-Carreras, I., Frise, E., Kaynig, V., Longair, M., Pietzsch, T., Preibisch, S., Rueden, C., Saalfeld, S., Schmid, B., Tinevez, J. Y., White, D. J., Hartenstein, V., Eliceiri, K., Tomancak, P. & Cardona, A. Fiji: an open-source platform for biological-image analysis. ***Nat. Methods*** 9, 676-682, (2012).

47 Contributors, N. napari: a multi-dimensional image viewer for Python. ***Zenodo https://doi. org/10.5281/zenodo*** 3555620, (2019).

Acknowledgments This work was supported by Laboratory Directed Research and Development Program LDRD21-013 and the U.S. Department of Energy (DOE), Office of Biological and Environmental Research as part of the Quantitative Plant Science Initiative at Brookhaven National Laboratory. The work used NSLS-II which is supported in part by the U.S. Department of Energy, Office of Science, Office of Basic Energy Sciences Program under contract number DESC0012704 (KC0401040).

Author contributions Y.Y., X. X., and Q.L. designed the study and experiments. Z. L., X. Z., Y.Y., and X. X. performed the experiments. All authors analyzed the data. Z. L. Y.Y, X. X. and Q.L. wrote the manuscript with help from other coauthors.

Competing interests Authors declare no competing interests.

Correspondence and requests for materials should be addressed to Y.Y., X.X, or Q.L.

Figures and captions

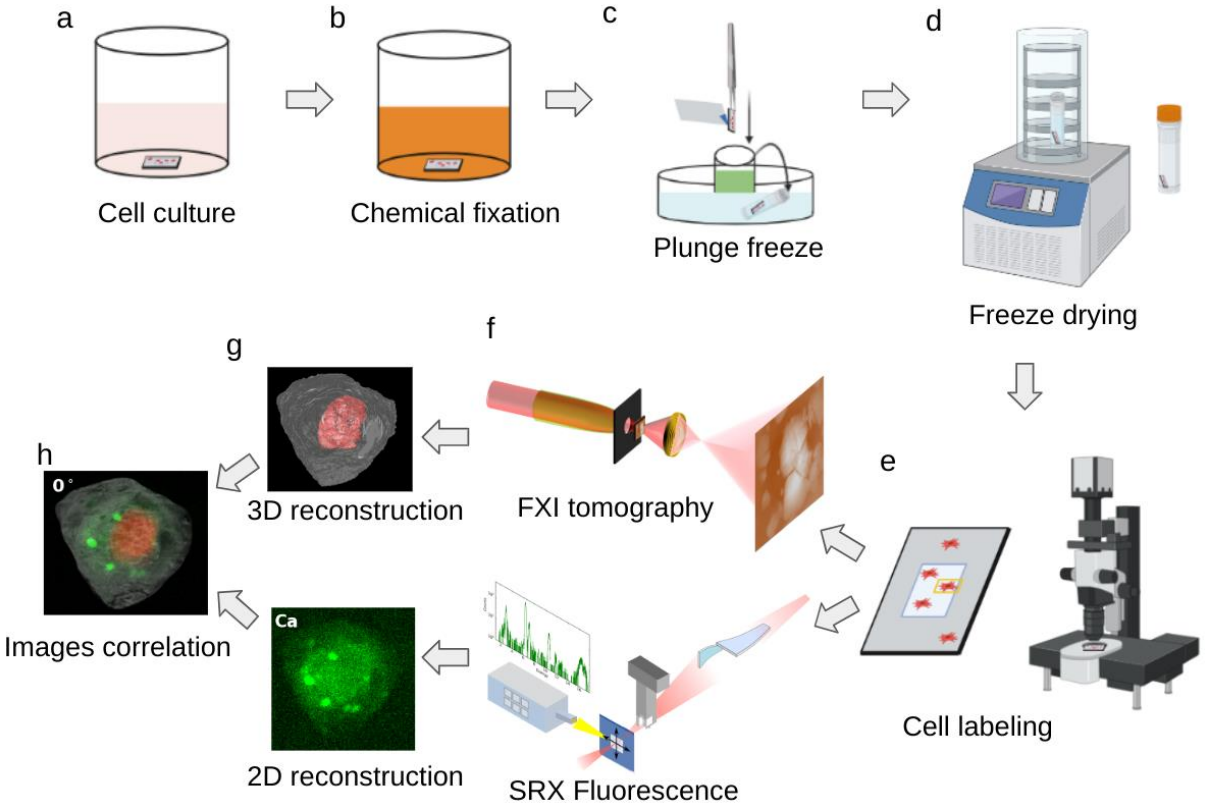

Fig. 1. Overall workflow of single-cell correlative X-ray imaging. **a**, HEK293T cells are grown adherently on the flat surface of a polylysine pretreated Si_3N_4 membrane. **b**, Media is removed twice PBS wash to wash out both media and floating dead cell. After that, a chemical fixation solution is added to fix the cell. **c**, Si_3N_4 membrane is washed twice with 150 mM ammonium acetate and then plunge-freeze via a Vitrobot. It is stored in a screw-cap microcentrifuge tube. **d**, The tube with the sample is moved to a freeze-dryer device for freezing-drying. **e**, Cells are labeled using confocal microscopy for multiple beamlines data collection. **f**, Single-cell data are collected using x-ray tomography at the FXI beamline and x-ray fluorescence microscopy at the SRX beamline, respectively. **g**, Reconstruction of 3D tomograms and 2D fluorescence map. **h**, Correlation of multimodality images.

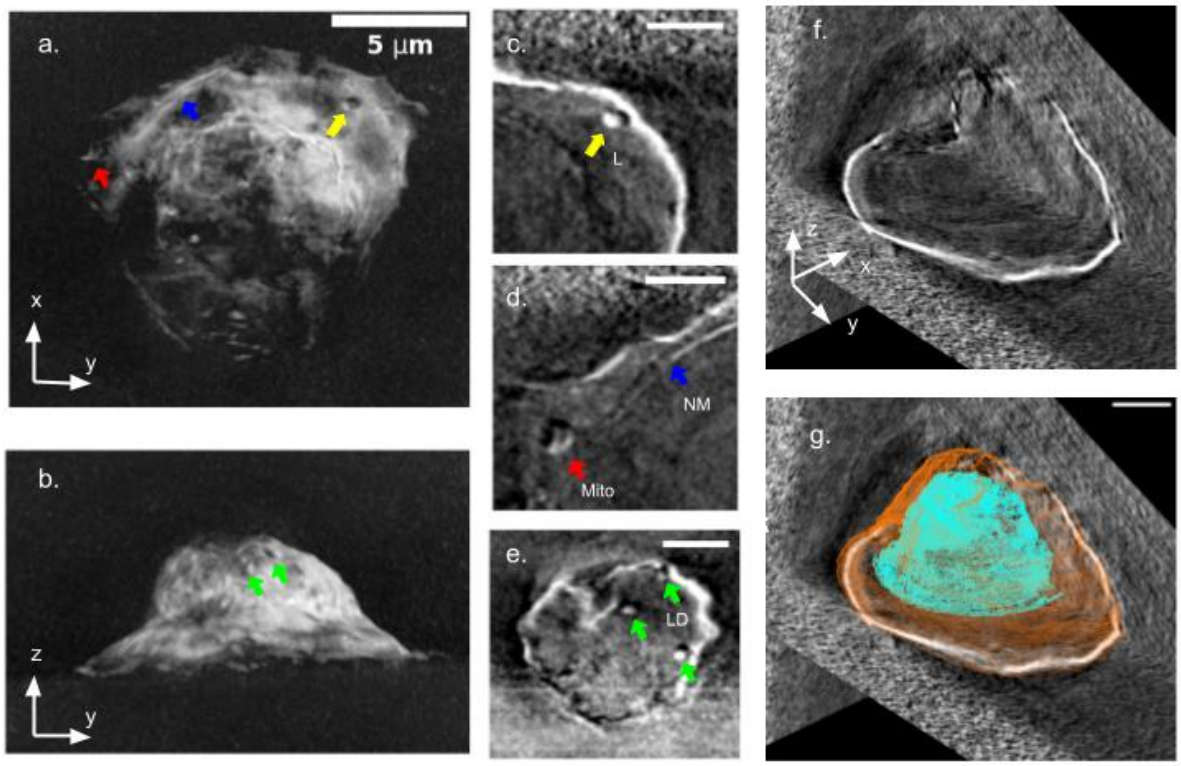

Fig. 2. Single-cell X-ray transmission tomography. Total projection of the reconstructed X-ray tomogram in XY (**a**) and YZ (**b**) directions. **c-e**, cellular structure features including mitochondrion (**c**), nucleus membrane (**d**), and lipid droplets (**e**). The diameter for lysosome (L, yellow), mitochondria (Mito, red), and lipid droplets (LD, green) are 500 nm, 800 nm, and 350 nm, respectively. **f**, Orthoslices of the cell along three directions. The whole cell is visualized in 3D (XY, YZ, and XZ) views. (**g**) View of f superimposed with the segmentation for nucleus (cyan) and plasma membrane (orange). Scale bar is 5 µm for **a** and **b, and** 2 µm for **c-g**.

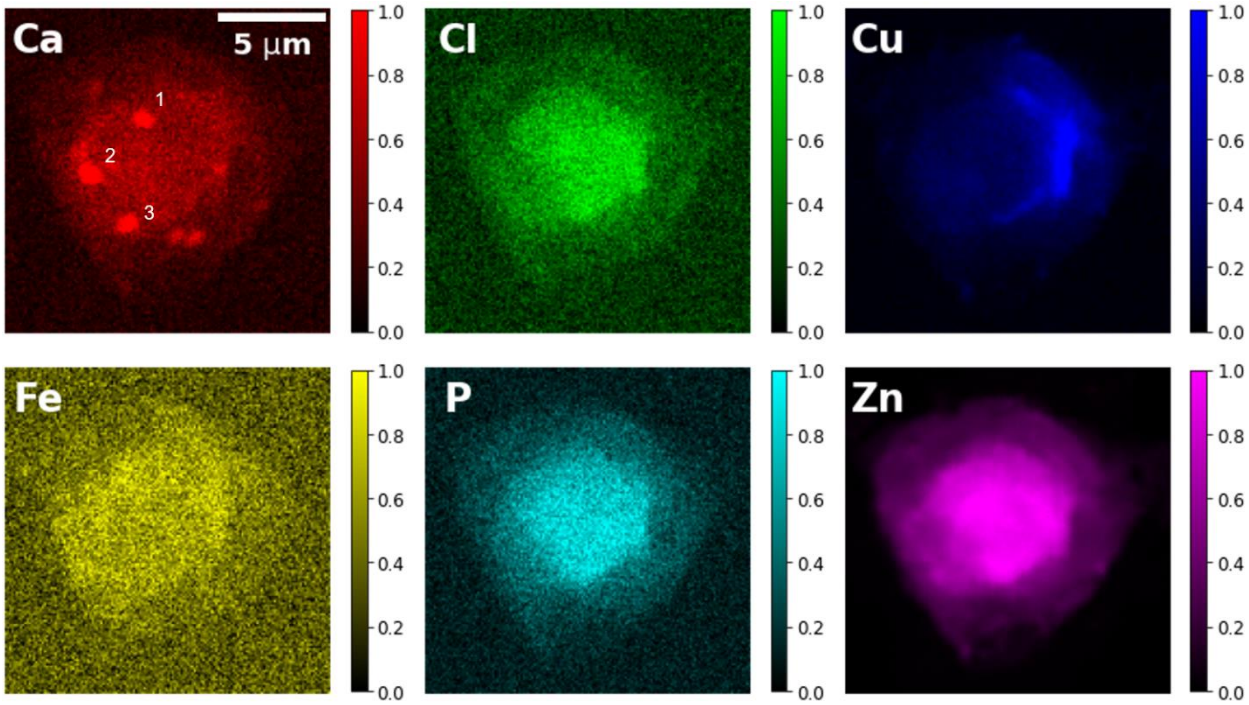

Fig. 3. X-ray fluorescence mapping of multiple chemical elements. The X-ray emission energy is 12 keV. Intensities are normalized for each component. The sizes of the three calcium-rich regions (labeled with numbers 1-3) are 1.0 μm,1.1 μm, 0.9 μm, respectively. Scale bar is 5 μm.

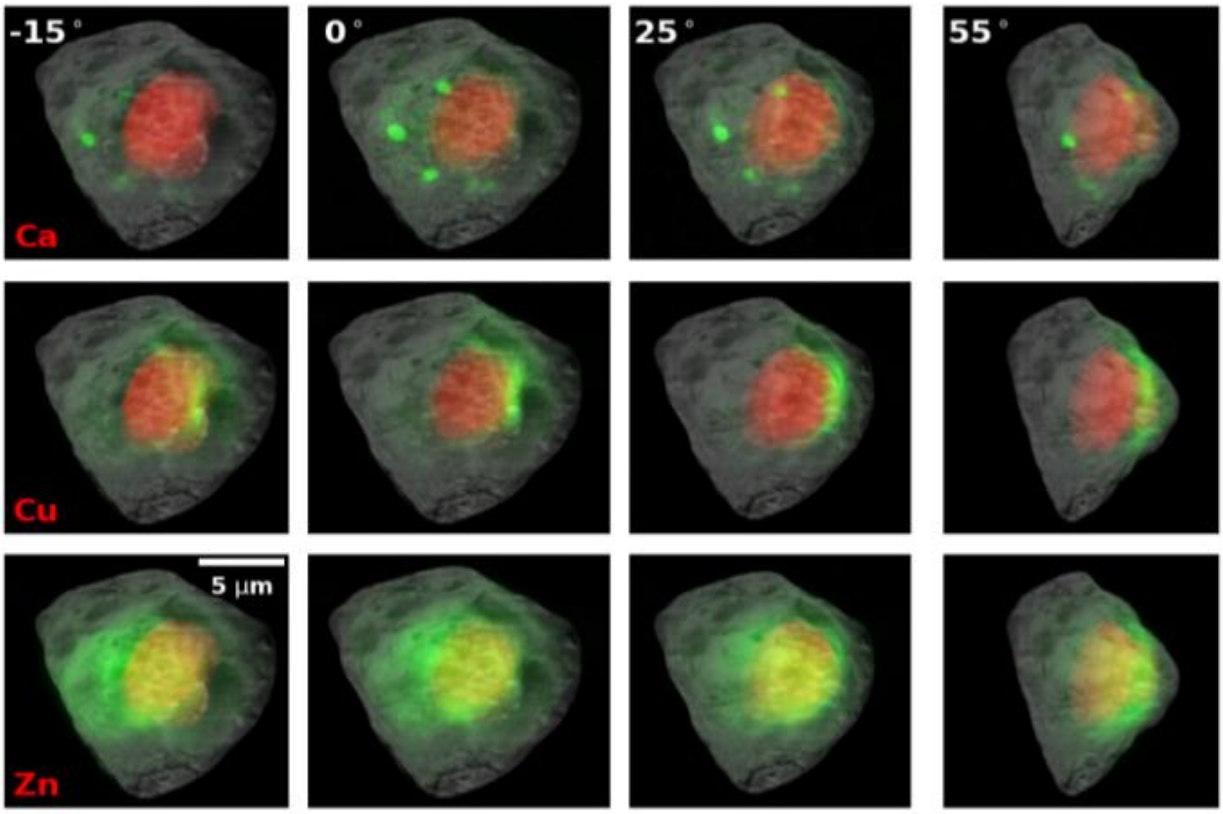

Fig. 4. Correlation of multi-modality data. Superimposition of 2D x-ray fluorescence (XRF) and 3D x-ray tomography (XRT) images along 4 different view angles. The cell was rotated along the y-axis by -15°, 0°, 25°, 55°, respectively. Gray scale maps show max projection of 3D x-ray tomography of the cells. Red masks show segmented nucleus from the X-ray tomography images. Green maps show the corresponding localization of multiple elements.

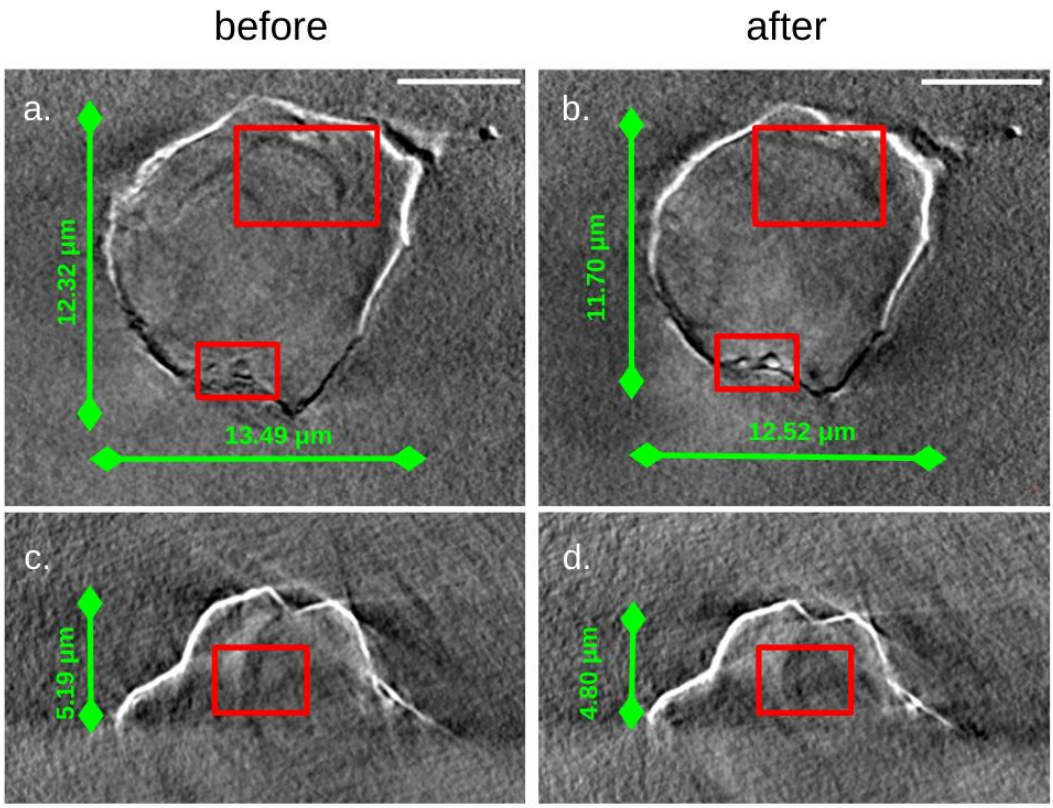

Fig. 5. Radiation damage in X-ray tomographic imaging. Representative slices of the reconstruction results of **a** and **c** from the first x-ray tomography scan and **b** and **d** from the last scan. FXI scan. The same experimental conditions are used for the first the last scans. Due to radiation damage, cell shrinkage is observed for three dimensions as labeled in blue. Scale bars are 5 µm.

Supplementary information

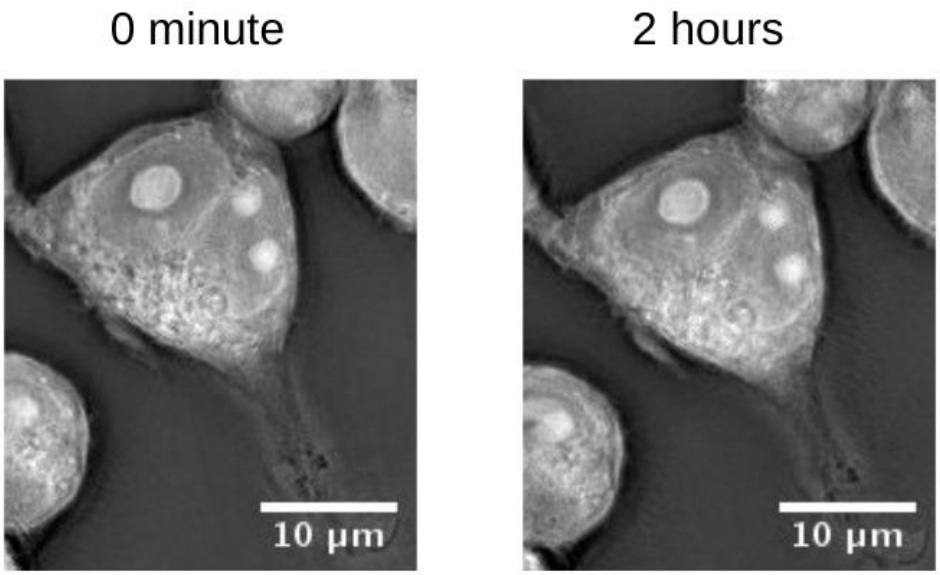

Supplementary Fig. 1. Nanolive cell imaging to monitor the PFA fixation process. The first and the last images of fixation imaging were selected to investigate the feature changes caused by the fixative. Some minor changes were observed such as the plasma membrane shrinkage on the top of the cell and the faded nucleus membrane. Although the fixative damage occurred, the overall cell structure didn't have a significant change in the 2-hour fixation.

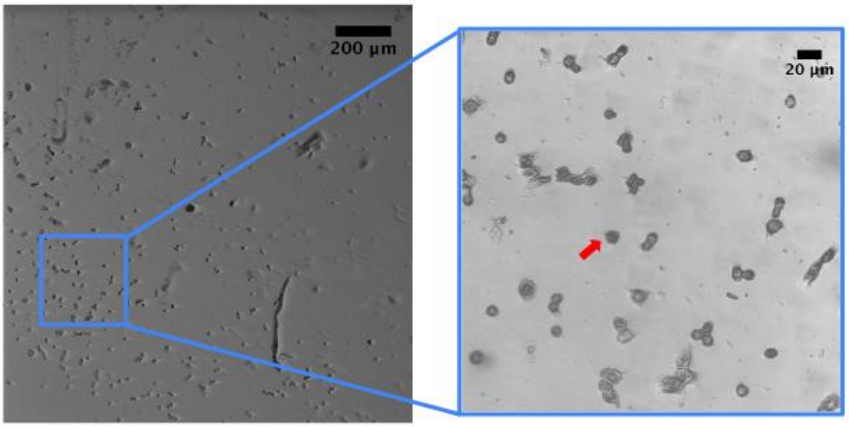

Supplementary Fig. 2. Multi-resolution confocal images for targeting and labeling cells for correlative multimodality x-ray imaging data collection. Both images played important roles in displaying the target cell location that provided a reference for X-ray imaging. Cell samples didn't require any pre-scan from an x-ray to find the target cell. A red arrow indicates the cell used for this study.

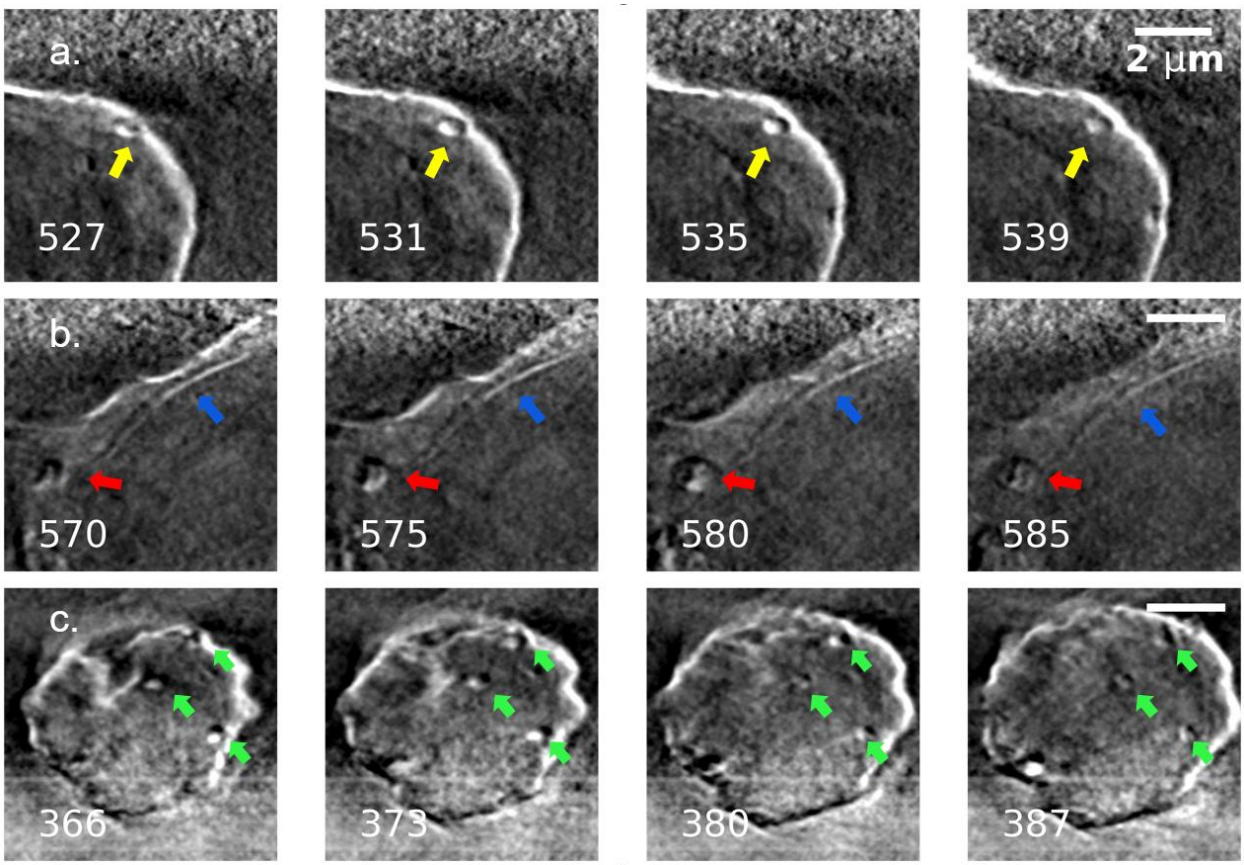

Supplementary Fig. 3. Representative slice views of intracellular organelles. lysosome (a, yellow), mitochondria (b, red) and nucleus membrane (b, blue), and lipid droplets (c, green) observed in the reconstructed tomogram. Scale bars are 2 μm. Numbers at the bottom left of each slice indicate the slice number in the 3D reconstructed tomogram. Each slice is 21.7 nm in thickness. Distance between the first slice and fourth slice for **a**, **b,** and **c** are 0.26 μm, 0.33 μm, 0.46 μm, respectively.

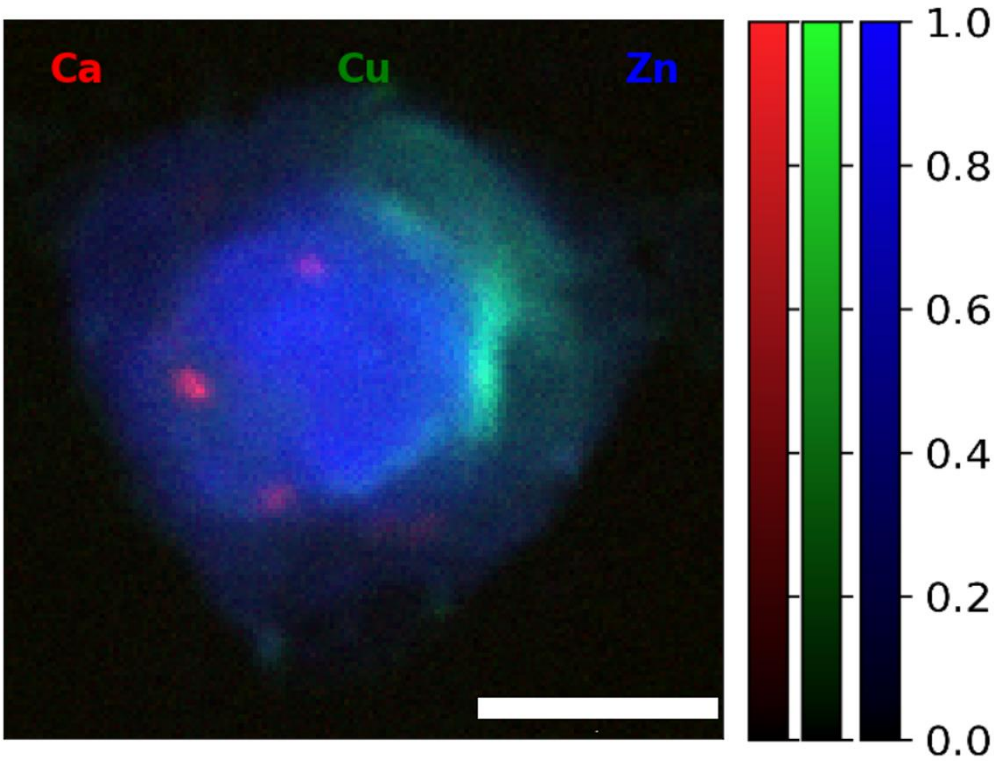

Supplementary Fig. 4. X-ray fluorescence imaging indicates relative localization of Ca, Cu, and Zn. Intensities are normalized for each component to showcase the relative amount in the cell. Scale bar is 5 μm.

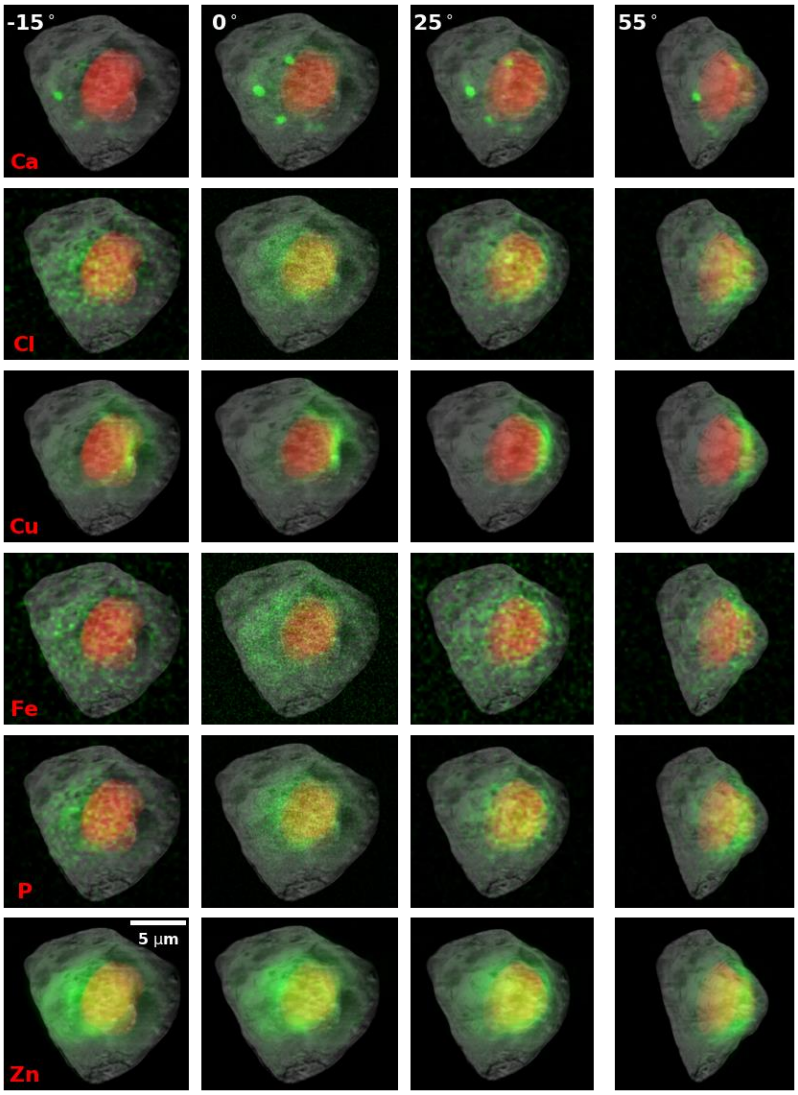

Supplementary Fig. 5. Correlation of multi-modality data. Superimposition of 2D SRX and 3D FXI single cell images along 4 different view angles. The cell was rotated along y-axis by -15°, 0°, 25°, 55°, respectively. Gray scale maps show max projection of 3D X-ray tomography of the cells. Red masks show segmented nucleus from 3D FXI images. Green maps show the corresponding localization of multiple chemical elements.

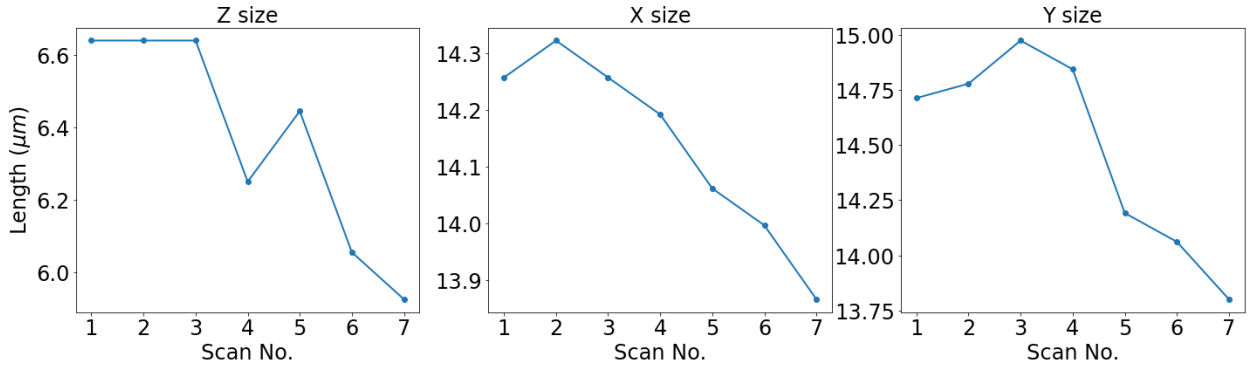

Supplementary Fig. 6. Cell size change caused by radiation damage. The size of the cell was measured in three orthogonal directions, namely, the Z, X, and Y axes, using the maximum length as the basis with respect to the number of TXM tomography scans. Panel abc illustrates the changes in size across seven different scans along the Z, X, and Y axes, respectively.

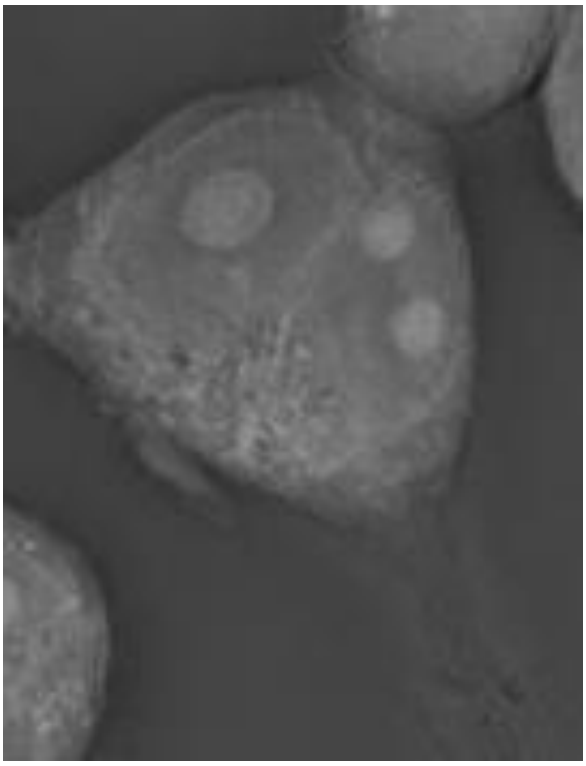

Supplementary Video 1. Live cell imaging to monitor the PFA fixation process.

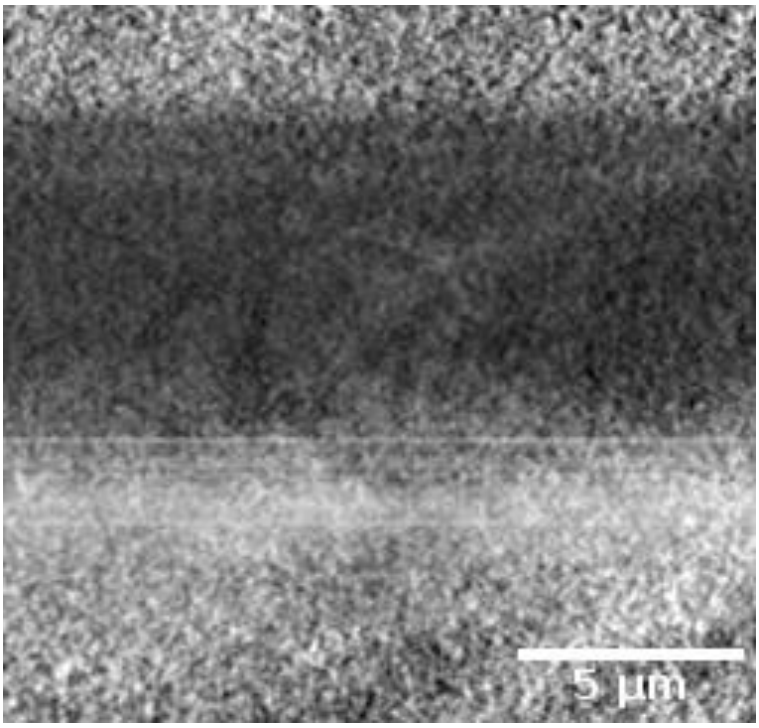

Supplementary Video 2. Sliced view of X-ray tomography from top of the cell to the bottom membrane support.